Supplementary information

Anaerobic neutrophilic pyrite oxidation by a chemolithoautotrophic nitrate-reducing iron(II)-oxidizing culture enriched from a fractured-aquifer

Natalia Jakus[a,b], Adrian Mellage[c], Carmen Hoeschen[d], Markus Maisch[a], James M. Byrne[a,e], Carsten W. Mueller[d,f], Peter Grathwohl[g] and Andreas Kappler[a]

[a]Geomicrobiology, Center for Applied Geoscience, University of Tuebingen, Germany

[b]Microbial Ecology, Center for Applied Geoscience, University of Tuebingen, Germany

[c]Hydrogeology, Center for Applied Geosciences, University of Tuebingen, Germany

[d]Soil Science, TUM School of Life Sciences, Technical University of Munich, Freising, Germany

[e]Now: School of Earth Sciences, University of Bristol, UK

[f]Now: Department of Geosciences and Natural Resource Management, University of Copenhagen, Denmark

[g]Hydrogeochemistry, Center for Applied Geoscience, University of Tuebingen, Germany

Number of pages: 23

Number of figures: 6

Number of tables: 3

Preparation and characterization of iron minerals

^{57}Fe-siderite and ^{NA}Fe-siderite (siderite with a natural abundance of iron isotopes) were synthetized using a 0.2 M stock solution of Fe^{2+} prepared by dissolution of 100% of ^{57}Fe-zero-valent iron (ZVI) (Chemgas™ France, ^{57}Fe content 97.83%) and ^{NA}Fe-ZVI (Alfa Aesar™, Germany, -200 mesh, 99% metals basis, natural abundance of Fe isotopes), respectively. To prepare stock solutions, 0.112 g of ZVI was transferred in a serum bottle into the glovebox (100% N_2) and left to deoxygenate for 1 day. After that, 10 ml of anoxic 1 M HCl was added to the bottle and stirred (500 rpm) overnight to dissolve the ZVI to obtain ca. 0.2 M Fe^{2+} solution. The Fe^{2+} solution was then poured into a clean glass beaker and, while stirring, the pH was adjusted to 6.0 using anoxic 5 M NaOH. The change of pH was followed by precipitation of green Fe(II) mineral phases. The precipitates were then removed by filtration through a 0.22 µm pore size syringe filter. The filtrate was poured into a beaker containing 10 ml of anoxic 0.21 M HCO_3^- solution and the pH was adjusted to 7.5-8.0 using anoxic 5 M NaOH, leading to precipitation of white crystals of siderite. The mineral suspension was then stirred for 3 more hours and left to settle overnight. Precipitates were washed three times with anoxic and sterile MQ water and collected on a 0.22 µm filter. The material was then re-suspended in 10 ml anoxic and sterile MQ to obtain a concentrated suspension of approximately 100 mM of Fe(II) in form of siderite.

Pyrite (pyrite with natural abundance of iron isotopes, ^{NA}Fe-FeS_2) was synthesized and purified following literature protocols.[1–3] All steps were performed under a continuous flow of N_2 under the fume hood and included washing by MQ, acetone and petroleum ether, and drying. The fraction below 0.63 mm was separated by sieving and stored dry in an oxygen-tight bottle until it was used in the experiments. The synthetized Fe(II) minerals were identified by X-ray diffraction (XRD) and Mössbauer spectroscopy (Fig. S1).

Solid phase treatment and Fe quantification

Batch incubations were sampled in an anoxic glovebox (100% N_2) by withdrawing 0.4 ml aliquots using sterile syringes. Samples were centrifuged (14,000 g, 10 min) to separate the supernatant from iron minerals and biomass. After centrifugation the supernatant was removed and 0.4 ml of 1 M HCl was added to the pellet (iron minerals and biomass) to dissolve all HCl-extractable iron (siderite and Fe(III) (oxyhydr)oxides). The samples were then shaken outside the glovebox at 1400 rpm at 25°C for 1 h (Eppendorf Thermomixer R Mixer). After extraction, the samples were diluted 1:3 with 1 M HCl. All measurements were performed in technical triplicate. Both Fe(II) and total Fe were quantified at 562 nm[4] using a microtiter plate reader (FlashScan 550, Analytic, Jena, Germany).

X-ray diffractometry (XRD) and Mössbauer spectroscopy

Samples for XRD analysis of siderite were collected from a stock mineral suspension and dried in an anoxic glovebox (100 % N_2) and together with a powdered pyrite sample kept in a glovebox until the measurements were done. XRD was performed using Bruker's D8 Discover GADDS XRD2 micro-diffractometer equipped with a standard sealed tube with a Co-anode (Co Kα radiation, $\lambda = 0.17903$ nm) at parameters of 30 kV/30 mA. The total time of measurement was 240 s at two detector positions (15 and 40°). Resulting diffractograms were analyzed using the software Match! (version 3.6.2.121).

Phase identification of iron minerals was performed using Mössbauer spectroscopy. Within an anoxic glovebox (100% N_2), mineral suspension samples taken from the batch incubation experiments were passed through a filter (0.45 µm, Millipore), sealed between two layers of

oxygen-impermeable adhesive polyimide film (Kapton), and kept frozen at -20°C in a sealed bottle until measurement. The sample was transferred to the instrument within an airtight bottle that was only removed prior to loading the samples inside the closed-cycle exchange gas cryostat (Janis cryogenics) under a backflow of helium. Measurements were collected at 77 K and 295 K with a constant acceleration drive system (WissEL) in transmission mode with a ^{57}Co/Rh source and calibrated against a 7 µm thick α-^{57}Fe foil measured at room temperature. All spectra were analyzed using Recoil (University of Ottawa) by applying a Voigt Based Fitting (VBF) site analysis. The half width at half maximum (HWHM) was fixed to a value of 0.12 mm/s for all samples. Absorbance spectra collected from biotic incubations (day 0, 8 and 146) were fitted with a 3-component model with fixed hyperfine parameters for pyrite (CS and QS of Db1, table S2) obtained from the reference pyrite material, but floating relative area to account for changes in the relative phase abundances in the analyzed samples.

XRD patterns and Mössbauer spectroscopy confirmed the synthesized minerals to consist of siderite (Fig. S1) and a mixture of pyrite and marcasite as previously described by [1,3]. Mössbauer parameters (Table S2) were more similar to values characteristic for marcasite instead of pyrite. However, both parameters are very close[5], and it is almost impossible to differentiate and quantify the abundance of both phases using Mössbauer spectroscopy. In the following we will therefore use pyrite as a general term for both minerals.

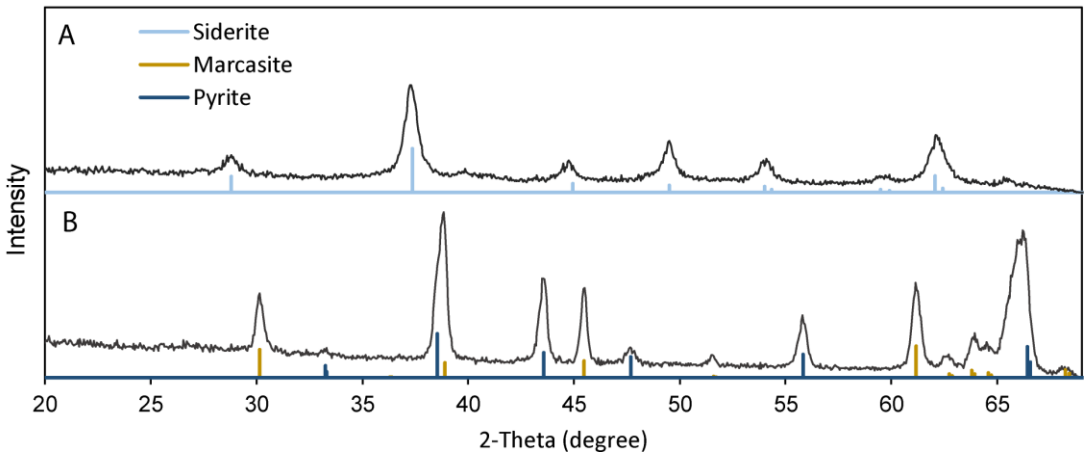

Fig. S1. XRD data of synthesized Fe(II) minerals used in this study. (A) synthesized siderite ($FeCO_3$) and (B) synthesized pyrite (FeS_2) containing some marcasite (FeS_2).

Quantification of elemental sulfur content

To quantify elemental sulfur in the solid phase, 0.1 g of synthesized FeS_2 was added to 50-mL glass serum bottles in triplicates, each containing 5 mL of cyclohexane and measured in technical duplicates. The suspensions were shaken for 3 h to extract elemental sulfur. Thereafter, an aliquot of 500 µL of each sample was collected and diluted further in 50 mL methanol, followed by dilution of the cyclohexane-methanol solution with a 1:9 mixture of methanol and MQ water to reach a final dilution of 1000x. The concentration of the elemental sulfur in the methanol filtrate was analyzed by HPLC (class VP with RID 10 A and DAD 457 SPD M 10A VP detectors (Shimadzu, Japan)) equipped with ReproSil-Pur 200 ODS-3 column (250 x 4 mm, 5 µm, Dr. Maisch GmbH, Germany), using 80% methanol in MQ as eluent. The sulfur concentration was determined using a calibration with Fluka™ Sulfur, purum p.a., ≥99.5%. The calibration standards were dissolved following the same procedure as was used to prepare samples. Despite extensive washing, some residual elemental sulfur was still present and was quantified after incubation of the synthetic pyrite in cyclohexane. The elemental sulfur content was 3.12±0.1 mass%.

Reaction model

Based on the conceptual model presented in the main manuscript and outlined in Fig. 1, we formulated a reaction model to fit the results from all experimental variants (without distinguishing between isotopically labeled vs. non-labeled siderite), thereby quantitatively testing our conceptual reaction network. The "batch reactor model" assumed well-mixed conditions in the incubations and neglected transport limitations.

Kinetic reaction rates for chemical equations 1, 2 and 3 were formulated assuming dual-Monod kinetics for biotic reactions and second-order kinetics for the abiotic Fe(III)-driven oxidation of pyrite. The dual-Monod rate formulations were biomass implicit, that is, without explicitly accounting for abundance of the NRFeOx culture because cell density was not monitored during the incubations. The rate of nitrate dependent siderite oxidation, r_{sidox} [mM d^{-1}], is given by:

$$r_{sidox} = r_{sidox}^{max}\left(\frac{C_{Sid}^{bio}}{K_{Fe(II)} + C_{Sid}^{bio}}\right)\left(\frac{C_{NO_3}}{K_{NO_3} + C_{NO_3}}\right) \quad (1)$$

where, r_{sidox}^{max} [mM d^{-1}], is the maximum rate of nitrate dependent siderite oxidation, $K_{Fe(II)}$ [mM] and K_{NO_3} [mM] are the half-saturation constants for Fe(II)-siderite and nitrate, respectively, C_{NO_3}[mM] is the concentration of dissolved nitrate and C_{Sid}^{bio} is the concentration of bioavailable Fe(II)-siderite. The model considers that only a fraction of the total Fe(II) in siderite is bioavailable, based on the observation that the concentration of HCl-extractable Fe(II) plateaus at ~1 mM. Thus, bioavailable Fe(II)-siderite was computed as:

$$C_{Sid}^{bio} = C_{Sid} - NB_{syd} \quad (2)$$

where NB_{syd} is the non-bioavailable concentration of siderite, assumed to be equal to the observed remaining concentration of HCl-extractable Fe(II). The approach is consistent with previous

considerations of bioavailable mineral fractions.[6] The governing processes controlling the observed bioavailability are discussed further in the Discussion section of the main manuscript.

Similarly, the rate of microbially-mediated pyrite oxidation was also parameterized based on a bio-available Fe(II)-pyrite concentration, C_{Pyr}^{bio} [mM], calculated based on the difference between the total pyrite concentration and a non-bioavailable amount, NB_{syd} [mM]. (Note: NB_{syd} is a fitting parameter, see Table S1).

$$r_{ndiox} = r_{ndiox}^{max}\left(\frac{C_{Pyr}^{bio}}{K_{Fe(II)} + C_{Pyr}^{bio}}\right)\left(\frac{C_{NO_3}}{K_{NO_3} + C_{NO_3}}\right) \quad (3)$$

In equation (3), r_{ndiox}^{max} [mM d^{-1}], is the maximum rate of nitrate-dependent pyrite oxidation. (Note: Identical values for the half-saturation coefficients $K_{Fe(II)}$ and K_{NO_3} were found to adequately depict the system behavior for all Fe(II)-mineral-nitrate reactive systems). As mentioned in the main manuscript, elemental sulfur, S^0, was initially present in incubations with pyrite, a direct artefact of the synthesis procedure. Because considerable sulfate production was measured throughout the experiments a contribution of S^0 oxidation coupled to NO_3^- reduction was also accounted for in the model:

$$r_{nsulf} = r_{nsulf}^{max}\left(\frac{C_{S(0)}}{K_{S(0)} + C_{S(0)}}\right)\left(\frac{C_{NO_3}}{K_{NO_3} + C_{NO_3}}\right) \quad (4)$$

where, r_{nsulf} and r_{sidox}^{max} [mM d^{-1}], the rate and maximum rate of S^0-dependent denitrification, $K_{S(0)}$ [mM] and K_{NO_3} [mM] are the half-saturation constants for S^0 and nitrate, respectively, and $C_{S(0)}$ [mM] is the concentration S^0.

Finally, the abiotic oxidation of pyrite by Fe(III) released from siderite oxidation (in mixed siderite and pyrite incubations) was parameterized as the second order rate expression, r_{pyrox} [mM d^{-1}]:

$$r_{pyrox} = k_{pyrox} \cdot C_{Pyr} \cdot C_{Fe(III)} \quad (5)$$

where k_{pyrox} [L mmol^{-1} s^{-1}] is the second-order rate constant of abiotic Fe(III)-mediated pyrite oxidation, and C_{Pyr} and $C_{Fe(III)}$ [mM], are the total (without considering a bioavailable fraction) concentrations of Fe(II)-pyrite and aqueous Fe^{3+}, respectively. The free Fe(II) released from the abiotic oxidation of pyrite could then serve as an additional source of electrons for further nitrate-dependent Fe(II) oxidation. In model Scenario 2 (S2), described in detail in the main manuscript, the rate of this additional contribution to denitrification was parameterized as r_{fedint}^{free} [mM d^{-1}], dependent on the concentration of dissolved ("free") Fe(II), $C_{Fe(II)}^{free}$ [mM], and for simplicity the same kinetic rate coefficients as for r_{ndiox} were used.

$$r_{fedenit}^{free} = r_{ndiox}^{max} \left(\frac{C_{Fe(II)}^{free}}{K_{Fe(II)} + C_{Fe(II)}^{free}} \right) \left(\frac{C_{NO_3}}{K_{NO_3} + C_{NO_3}} \right) \quad (6)$$

Considering the above reaction rate expressions, the well-mixed reactor model yields the following system(s) of governing ordinary differential equations the (1) siderite-only, (2) pyrite-only, and (3) mixed pyrite-siderite biotic experiments:

1) Siderite only

$$\frac{dC_{NO_3}}{dt} = -r_{sidox} \quad (7)$$

$$\frac{dC_{Sid}}{dt} = -5 \cdot r_{sidox} \quad (8)$$

$$\frac{dC_{Fe(III)}}{dt} = 5 \cdot r_{sidox} \quad (9)$$

2) Pyrite only

$$\frac{dC_{NO_3}}{dt} = -3 \cdot r_{ndiox} - 1.2 \cdot r_{nsulf} \quad (10)$$

$$\frac{dC_{Pyr}}{dt} = -r_{ndiox} \quad (11)$$

$$\frac{dC_{Fe(III)}}{dt} = r_{ndiox} \quad (12)$$

$$\frac{dC_{S(0)}}{dt} = -r_{nsulf} \quad (13)$$

$$\frac{dC_{SO_4}}{dt} = 2 \cdot r_{ndiox} + r_{nsulf} \quad (14)$$

3) Mixed pyrite and siderite

$$\frac{dC_{NO_3}}{dt} = -r_{sidox} - 3 \cdot r_{ndiox} - 1.2 \cdot r_{nsulf} - \boldsymbol{r_{fedint}^{free}} \quad (15)$$

$$\frac{dC_{Sid}}{dt} = -5 \cdot r_{sidox} \quad (16)$$

$$\frac{dC_{Fe(II)}}{dt} = \mathbf{14} \cdot \boldsymbol{r_{pyrox}} - \mathbf{5} \cdot \boldsymbol{r_{fedint}^{free}} \quad (17)$$

$$\frac{dC_{Fe(III)}}{dt} = r_{ndiox} + 5 \cdot r_{sidox} + \mathbf{5} \cdot \boldsymbol{r_{fedint}^{free}} - \mathbf{14} \cdot \boldsymbol{r_{pyrox}} \quad (18)$$

$$\frac{dC_{Pyr}}{dt} = -r_{ndiox} - \boldsymbol{r_{pyrox}} \quad (19)$$

$$\frac{dC_{S(0)}}{dt} = -r_{nsulf} \quad (20)$$

$$\frac{dC_{SO_4}}{dt} = 2 \cdot r_{ndiox} + r_{nsulf} + \mathbf{2} \cdot \boldsymbol{r_{pyrox}} \quad (21)$$

The terms in bold font in equations 16, 17 and 19 mark the distinction between model versions that consider both biotic and abiotic pyrite oxidation (i.e., including all terms) versus biotic pyrite oxidation only (i.e., not including the terms in bold). The systems of ordinary differential equations were solved using ode15s in MATLAB. The model was calibrated by fitting the parameters to the experimental data of the siderite- and pyrite-only cases jointly, as these allowed to separate the reactive contributions of siderite and pyrite from one another, which were then lumped in a

validation step of the "mixed" experiment. Fitting was performed on the logarithmized parameter values using the trust-region-reflective algorithm in the MATLAB least squares optimization function *lsqnonlin*[7], minimizing the sum of squared error between measurements and model output. The calibrated parameter set yielded a root mean squared error (RMSE) of 0.01 mM, well within the standard deviation of the measurements. Model parameter values are presented in Table S1.

Table S1. Calibrated parameter values for the reaction model versions described above.

Parameter	Unit	Value	Fitted
r_{sidox}^{max}	[mM s^{-1}]	1.82e-5	*
r_{ndiox}^{max}	[mM s^{-1}]	1.65e-6	*
r_{nsulf}^{max}	[mM s^{-1}]	1.32e-6	*
$K_{Fe(II)}^{sid}$	[mM]	20	*
$K_{Fe(II)}^{pyr}$	[mM]	1.43	*
$K_{NO_3}^{Fe}$	[mM]	0.25	*
$K_{NO_3}^{S}$	[mM]	0.15	*
$K_{S(0)}$	[mM]	1.73	*
k_{pyrox}	[L mmol s^{-1}]	1e-8	[a]
NB_{sid}	[mM]	1 – 1.15	[b]
NB_{pyr}	[mM]	4.91	*

*Fitted. [a]Not fitted, taken as the HCl-extractable iron remaining in each treatment. [b]Arbitrary value to illustrate that even a small contribution of abiotic pyrite oxidation would over-predict nitrate reduction.

NanoSIMS

NanoSIMS analyses were performed at the Cameca NanoSIMS 50L at the Institute of Interdisciplinary Research on Environment and Materials (IPREM) (UPPA, Pau, France) with courtesy of Cameca, France. Prior to the measurements, the samples were coated with a Pd layer (~12 nm) to avoid charging during the SEM analysis. The O^- and Cs^+ primary ion beams were used with a primary ion impact energy of 16 keV. Prior to the final measurement, any potential contaminants and the coating layer were sputtered away with a high primary beam current (pre-sputtering). The primary beam (~3 pA for O^- and ~1pA for Cs^+) was focused and scanned over the sample with $^{56}Fe^+$, $^{57}Fe^+$ (O^- beam) and $^{56}Fe^{16}O$, ^{32}S (Cs^+ beam) secondary ions collected using electron multipliers. All analyses were performed in imaging mode, on samples from the treatments containing 1) ^{NA}Fe-pyrite, ^{57}Fe-siderite and bacterial cells (biotic control), 2) ^{NA}Fe-pyrite, ^{NA}Fe-siderite and bacterial cells (control for isotopic enrichment), and 3) ^{NA}Fe-pyrite, ^{57}Fe-siderite and autoclaved bacterial cells (abiotic control). For every treatment, four representative spots were analyzed for the spatial distribution of ^{56}Fe mainly originating from pyrite and ^{57}Fe mainly derived from siderite taking advantage of the high spatial resolution of the new RF plasma O source. To follow the sulfur distribution (^{32}S), due to the pure ionization in O^- polarity, the Cs^+ primary beam of the NanoSIMS instrument was used, at similar spatial resolution (~100 nm). In this configuration iron isotopes can be measured as ^{56}FeO and ^{57}FeO. Images of 20 µm x 20 µm (O^- beam) and 25 µm x 25 µm (Cs^+ beam) field of view, 30 and 20 planes respectively with a dwell time of 1 ms/pixel, 256 pixels x 256 pixels were recorded. The NanoSIMS images were analyzed using the Open MIMS Image plugin available within ImageJ (available free-of-charge at, https:// imagej.nih.gov/ij/). All presented images were corrected for the electron multiplier dead time (44 ns), as well as drift corrected, and the planes accumulated.

Enrichment and cultivation of microorganisms

Briefly, 10 cm-long pieces of Teflon tubing were filled with crushed pyrite-rich Upper Muschelkalk limestone representative for the aquifer and deployed in one of groundwater monitoring wells. After 4 months of incubation, exposed rock particles were retrieved from the well and added to anoxic bicarbonate-buffered (22 mM) freshwater low phosphate medium (LPM) modified from Ehrenreich & Widdel[8] containing 0.6 g/L KH_2PO_4, 0.3 g/L NH_4Cl, 0.5 g/L $MgSO_4 \cdot 7H_2O$, and 0.1 g/L $CaCl_2 \cdot 2H_2O$, adjusted to pH 7.1, amended with 2 mM of $NaNO_3$ and 2 mM of $FeCl_2$. The concentration of selenite–tungstate solution (Widdel, 1980) was decreased from 1.0 mL/L to a final concentration of 0.1 mL/L to eliminate a potential inhibitory effect of tungsten on the nitrate reductase (Burke, Calder and Lascelles, 1980). The enrichment culture has a genetic potential to perform pyrite oxidation as it is dominated by a potential Fe(II)-oxidizer belonging to the *Gallionellaceae* family, among which some species also have nitrate reductases (He et al., 2016) and thiosulfate oxidases (Emerson et al., 2013), accompanied by bacteria affiliated with *Acidovorax* spp., *Dechloromonas* spp. and *Bradyrhizobium* spp., known heterotrophic nitrate-reducers (Coates et al., 2001; Polcyn and Luciński, 2003; Heylen, Lebbe and de Vos, 2008; Siqueira, Minamisawa and Sánchez, 2017) and bacteria belonging to *Thiobacillus* family, having potential for sulfur oxidation. After 36 continuous transfers under autotrophic conditions (no organic carbon added) the enrichment NRFeOx culture was used as inoculum in the batch incubation experiments described below.

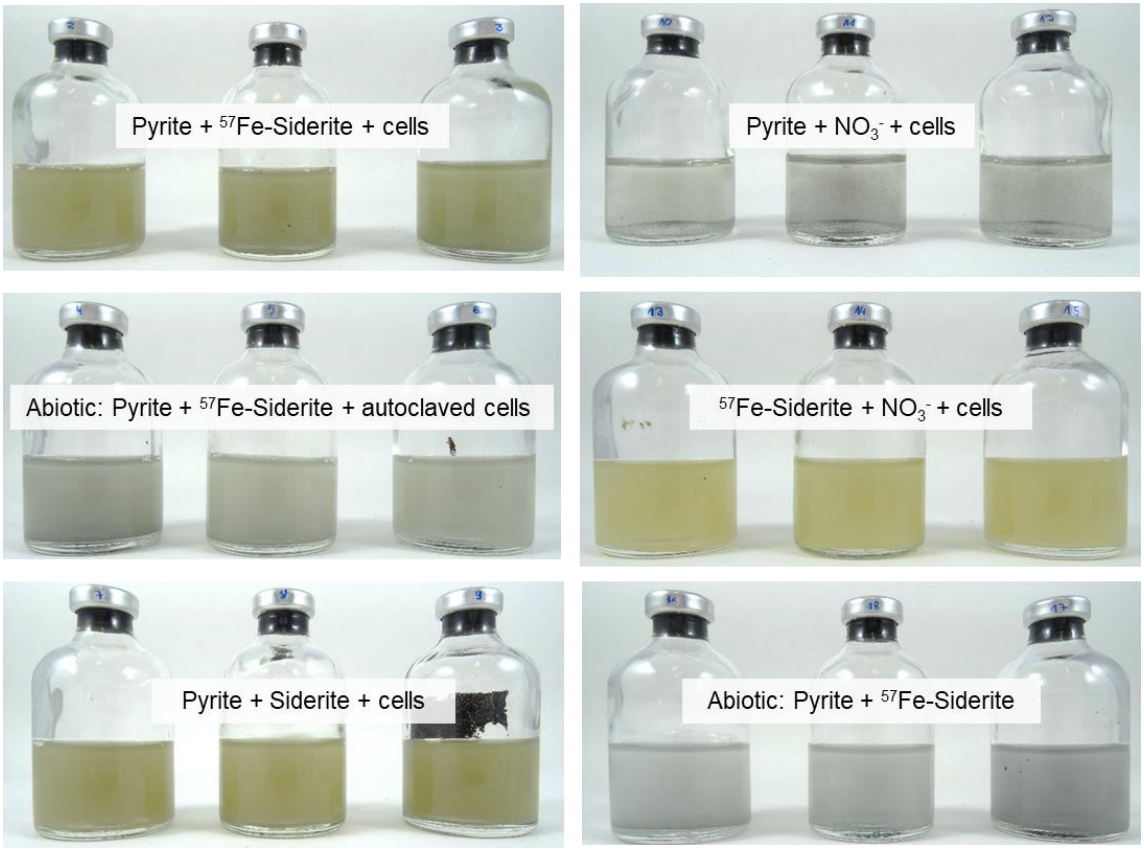

Fig. S2. Photographs of experimental bottles containing various combinations of pyrite, ^{57}Fe-labelled or non-labelled siderite and cells. Photos were taken at day 8 (when the bottles were sampled for NanoSIMS analysis).

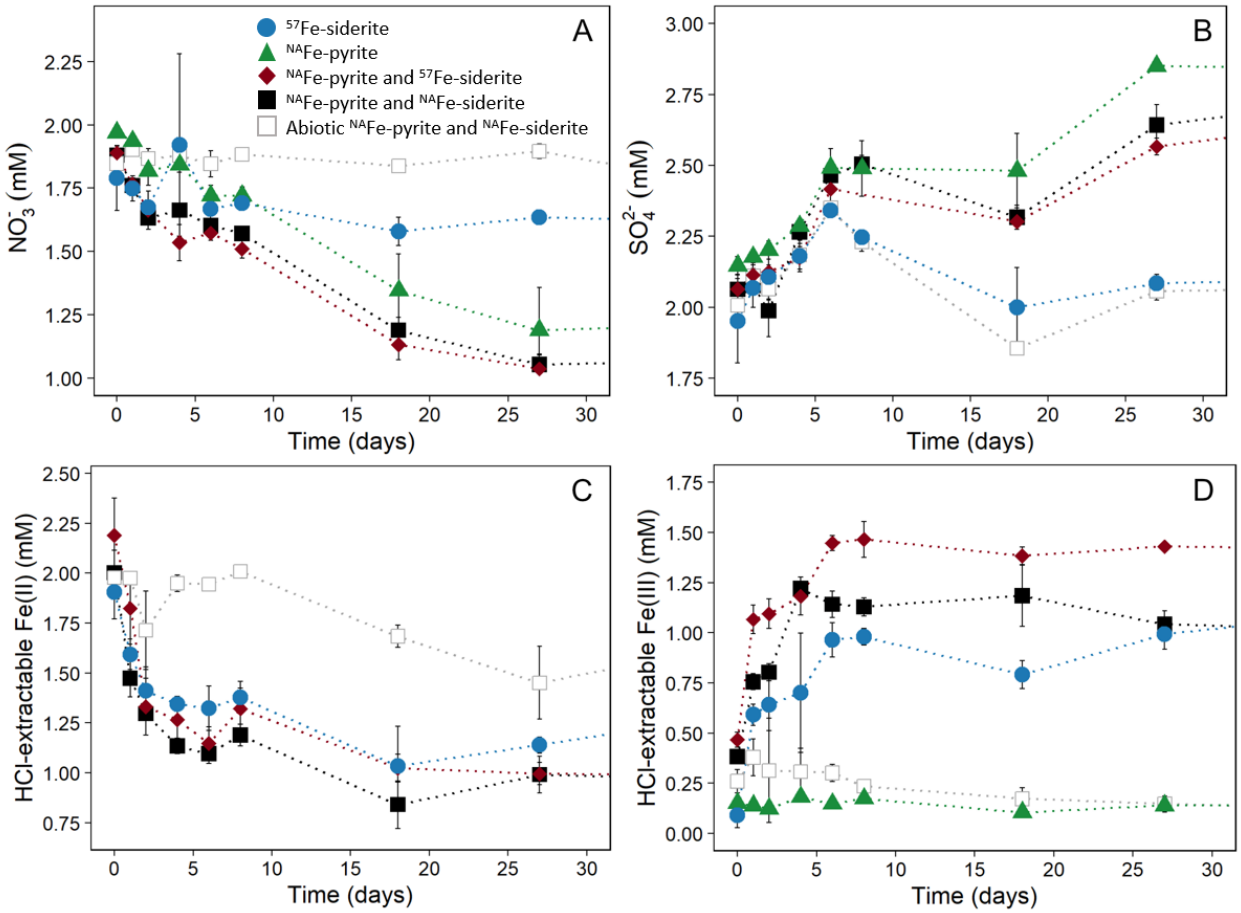

Fig. S3. Nitrate (A), sulfate (B), HCl-extractable Fe(II) (C) and Fe(III) concentration (D) within the first 30 days of the experiment in setups where the autotrophic NRFeOx enrichment culture was incubated with nitrate and ^{57}Fe-siderite (blue circles), ^{NA}Fe-pyrite (green triangles), both ^{NA}Fe-pyrite and either or ^{57}Fe-siderite (black squares) or ^{NA}Fe-siderite (red diamonds) under anoxic, pH-neutral conditions. Abiotic controls contained 10% vol. of the same culture that was inactivated by autoclaving. All data points are average values of samples from three independent biological replicates, error bars represent standard deviations. Please note that in the setup containing only ^{NA}Fe-pyrite no Fe(II) could be measured due to the low solubility of pyrite in 1 M HCl.

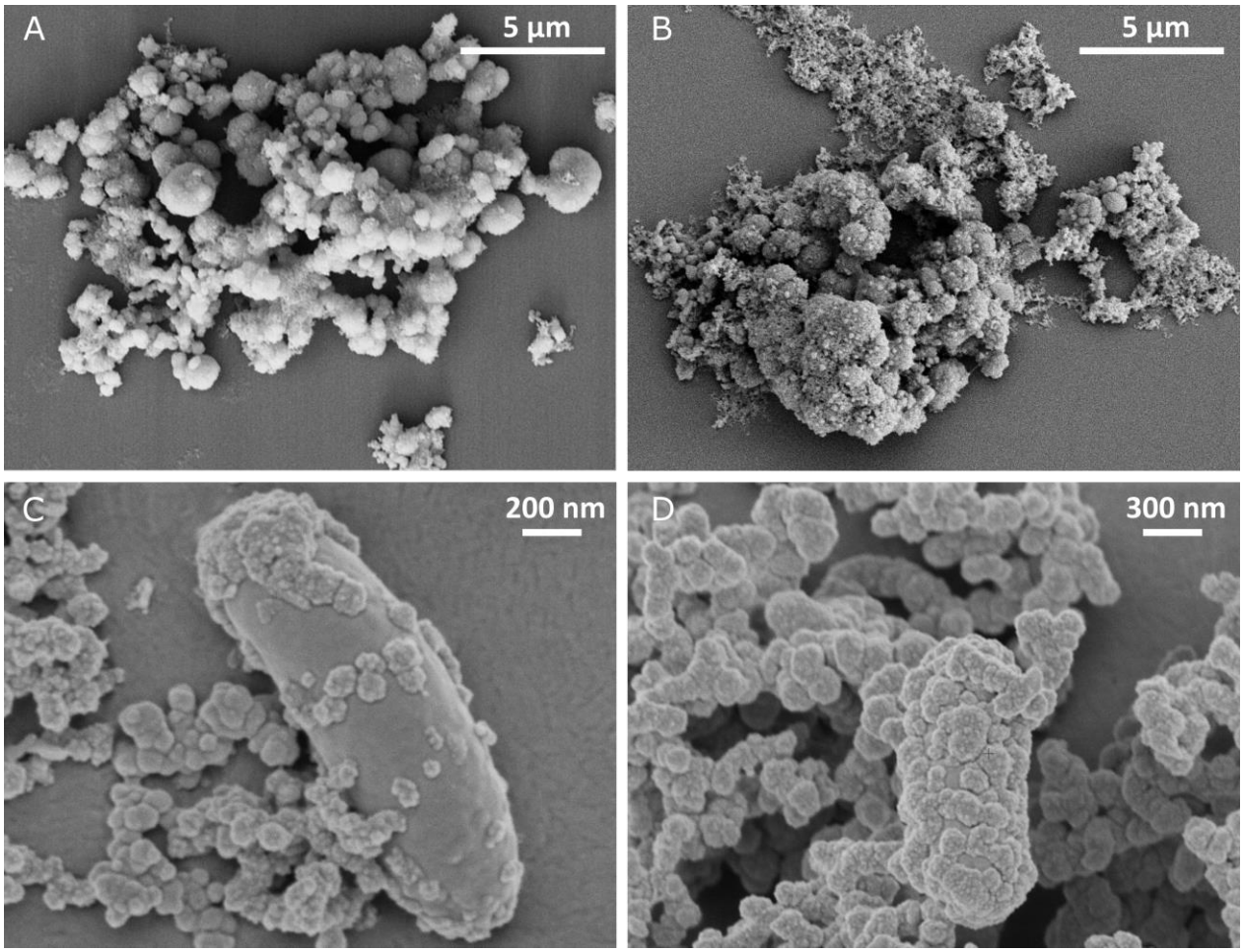

Fig. S4. Scanning electron micrographs of cell-mineral aggregates from setups containing both pyrite and ^{57}Fe-siderite incubated with autoclaved bacterial cells (A) and active bacterial cells (B) at day 8 of the experiment. Images of encrusted bacterial cells (C) and (D) collected at day 8 from setups that contained both pyrite and siderite and living cells.

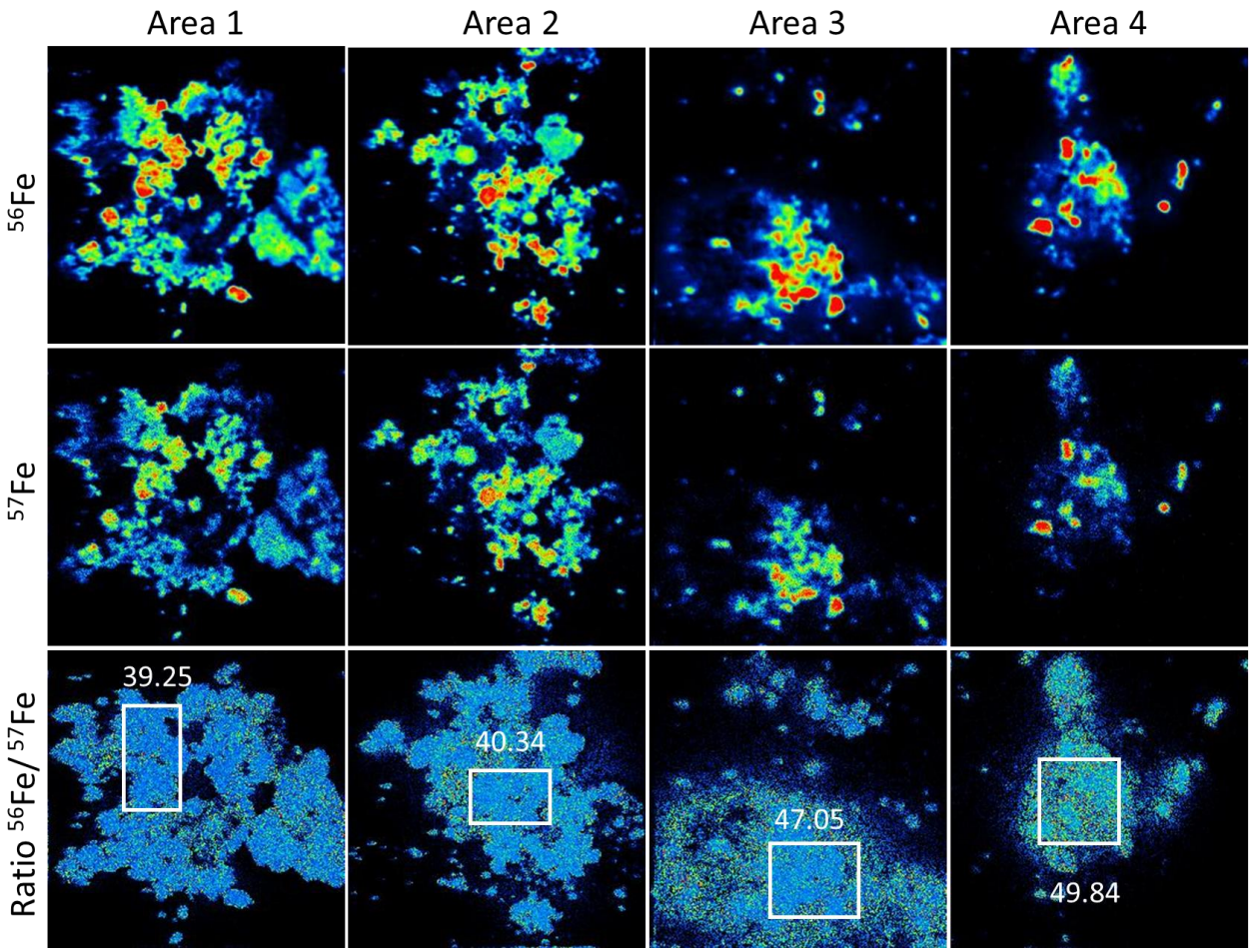

Fig. S5. High spatial resolution NanoSIMS analysis of two isotopes of iron: ^{56}Fe (1st row) and ^{57}Fe (2nd row) of 4 different areas containing mineral aggregates. All images were collected at the 8th day of incubation of ^{NA}Fe-siderite and ^{NA}Fe-pyrite with NRFeOx culture. The homogenous distribution iron isotopes is demonstrated by ratio image ^{56}Fe/^{57}Fe (3rd row). White boxes are indicating areas in which particular ratio was calculated while the numbers are showing the calculated value. All ratios exhibit a close value to theoretical ^{56}Fe/^{57}Fe ratio for natural abundance of iron isotopes (91.75/2.21 = 43.28).

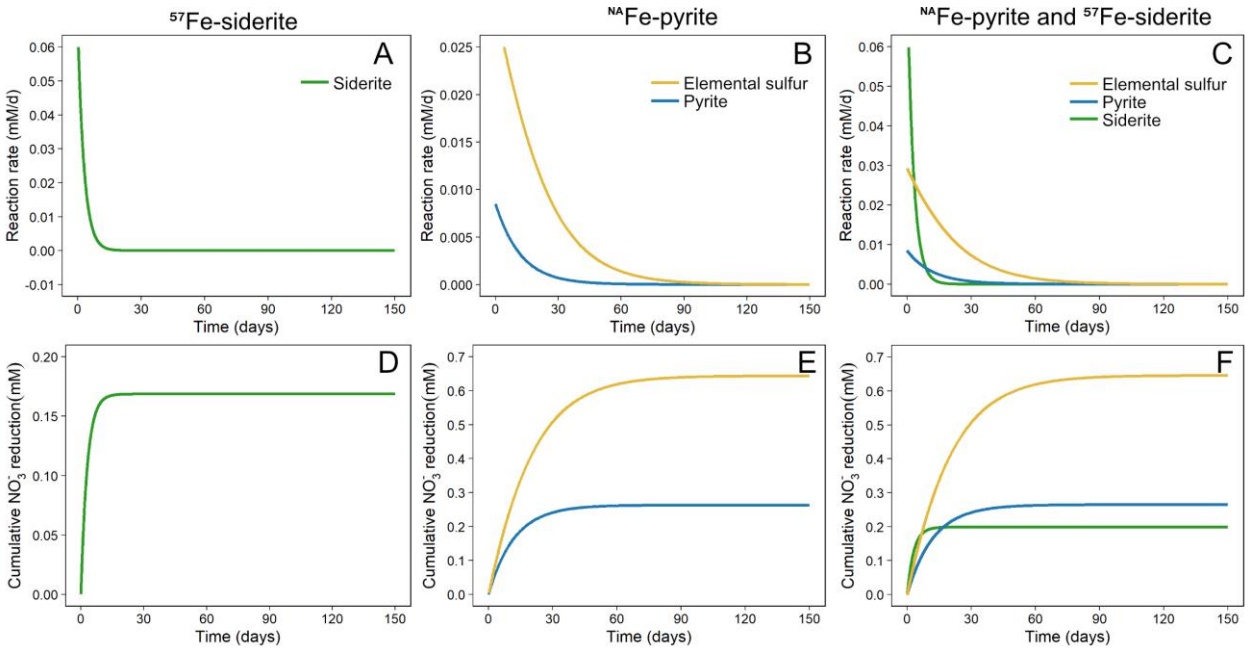

Fig. S6. Reaction rates of microbially-mediated siderite oxidation (green), elemental sulfur oxidation (yellow) and pyrite oxidation (blue). Cumulative nitrate reduction (mM) coupled to siderite oxidation (green), elemental sulfur oxidation (yellow) and pyrite oxidation (blue).

Table S2. Mass balance of substrates and products of the reaction in setups initially containing 2 mM NO_3^- and 5 mM of Fe(II) in form of FeS_2 together with 0.54 mM S^0 and/or 2 mM of Fe(II) in form of $FeCO_3$ incubated with our lithoautotrophic NRFeOx enrichment culture under anoxic, pH-neutral conditions.

	NO_3^- reduced (mM)	HCl-extractable Fe(II) remaining the in solids (mM)	Final Fe^{2+} (aq)	Fe(II) absorbed to glass walls (mM)	HCl-extractable Fe(II) depleted (mM)*	Fe(III) formed (mM)	SO_4^{2-} formed (mM)	Ratio NO_3^- $_{reduced}$/ $SO_4^{2-}{}_{formed}$	Ratio NO_3^- $_{reduced}$/ $Fe(III)_{formed}$
^{57}Fe-Siderite	0.16 ± 0.13	1.11 ± 0.08	0.01 ± 0.00	0.02 ± 0.00	0.78 ± 0.1	1.28 ± 0.2	0.11 ± 0.15	-	0.2 ± 0.04
Pyrite	0.79 ± 0.19	0.00 ± 0.00	0.01 ± 0.00	0 .00 ± 0.00	0.00 ± 0.01	0.01 ± 0.04	0.72 ± 0.2	1.11 ± 0.04	-
Pyrite and ^{57}Fe-Siderite	0.84 ± 0.04	0.89 ± 0.04	0.04 ± 0.01	0.01 ± 0.00	1.11 ± 0.08	0.94 ± 0.07	0.60 ± 0.08	1.41 ± 0.12	0.89 ± 0.05
Pyrite ^{NA}Fe-Siderite	0.90 ± 0.06	0.78 ± 0.12	0.02 ± 0.01	0.01 ± 0.00	1.40 ± 0.14	1.09 ± 0.14	0.61 ± 0.07	1.49 ± 0.17	0.85 ± 0.16
Abiotic control	0.00 ± 0.01	1.67 ± 0.16	0.21 ± 0.02	0.31 ± 0.06	0.31 ± 0.29	0.03 ± 0.07	0.1 ± 0.03	-	-

*Calculated as final concentration of Fe(II) extracted from solids subtracted from initial concentration of Fe(II) extracted from solids. This fraction represents the amount of Fe(II) removed by oxidation and dissolution from the Fe(II) solids at the beginning of experiment.

Table S3. Overview on Mössbauer spectra fitting parameters. Temp. – temperature during measurement; Phase – fitted compound, Db: doublet, center shift (CS in mm/s); quadrupole splitting (ΔEQ in mm/s); sigma – deviation/broadening of the quadrupole splitting fit. quadrupole shift (ε in mm/s); hyperfine field (Bhf in T), Pop – relative abundance (in %), χ2 as goodness of fit and identified (iron) mineral phases.

Sample	**Temp. K**	**Phase**	**CS mm/s**	**ΔE_Q mm/s**	**sigma mm/s**	**Pop (±) %**	**χ^2**	**Fe phase**
^{NA}Fe-Pyrite	77	Db1	0.34	0.52	0.18	100 (0.3)	0.61	Pyr
	5	Db1	0.36	0.52	0.08	100 (0.2)	0.54	Pyr
^{NA}Fe-Pyrite + ^{57}Fe-Siderite + cells (day 0)	77	Db1	0.34	0.52	0.19	5.2 (1.3)	0.62	Pyr
	77	Db2	1.34	2.40	0.81	94.2 (1.2)		Sid
	77	Db3	0.43	0.74	0.20	0.6 (0.2)		Fe(III)
^{NA}Fe-Pyrite + ^{57}Fe-Siderite + cells (day 8)	77	Db1	0.34	0.52	0.25	13.8 (1.5)	3.65	Pyr
	77	Db2	1.33	2.36	0.49	53.1 (1.3)		Sid
	77	Db3	0.50	0.80	0.39	33.1 (1.6)		Fe(III)
^{NA}Fe-Pyrite + ^{57}Fe-Siderite + cells (day 146)	77	Db1	0.34	0.52	0.24	12.0 (1.5)	3.78	Pyr
		Db2	1.23	2.24	0.48	46.6 (1.9)		Sid
		Db3	0.50	0.79	0.36	43.4 (1.4)		F(III)
Abiotic (no cells) ^{NA}Fe-Pyrite + ^{57}Fe-Siderite (day 0)	77	Db1	0.34	0.52	0.21	5.4 (0.14)	0.65	Pyr
		Db2	1.22	2.39	0.41	94.6 (0.81)		Sid
Abiotic (no cells) ^{NA}Fe-Pyrite +^{57}Fe-Siderite (day 8)	77	Db1	0.34	0.52	0.19	5.6 (0.21)	0.64	Pyr
		Db2	1.21	2.36	0.39	94.4 (0.48)		Sid

Additional stoichiometric calculations

The culture used in our study was described to perform complete denitrification with a $nitrate_{reduced}$:$Fe(II)_{oxidized}$ ratio close to the expected stochiometric ratio of 0.2 (Jakus et al, in revision) following equation (1).

$$10Fe^{2+} + 2NO_3^- + 24H_2O \rightarrow 10Fe(OH)_3 + N_2 + 18H^+ \qquad (1)$$

Herein, we calculated the stoichiometric ratio based on measured Fe(III) concentrations (representing $Fe(II)_{oxidized}$) because of the sorption of Fe(II) discussed in the manuscript. For setups with only ^{57}Fe-siderite and nitrate, the calculated ratio of $nitrate_{reduced}$:$Fe(III)_{formed}$ was 0.2±0.04 (Table S2). Thus, equaling the theoretical ratio for Fe(II) oxidation coupled to complete denitrification to N_2. However, in microcosms where both pyrite and ^{57}Fe-siderite or pyrite and ^{NA}Fe-siderite were present, the ratios were much higher (0.89±0.05 and 0.85±0.16, respectively), suggesting that more nitrate was reduced than expected based on the measured Fe(III) produced. This is in line with the modelled contribution of S^0-dependent denitrification, which adequately captured the trends in concentration time series. Based on equation (2) and the presence of 3.12±0.1 mass% S^0 associated with our pyrite, a maximum of 0.54 mM of sulfate could be formed and 0.7 mM of nitrate reduced in agreement the higher $nitrate_{reduced}$:$Fe(III)_{formed}$ ratio.

$$S^0 + 1.2NO_3^- + 0.4H_2O \rightarrow SO_4^{2-} + 0.6N_2 + 0.8H^+ \qquad (2)$$

We also estimated the maximum amount of pyrite which could be potentially oxidized by Fe^{3+} originating from siderite oxidation coupled to nitrate reduction, assuming that all HCl-extractable siderite-Fe(II) could be oxidized by bacteria to Fe^{3+}(aq). Following equation (3) and considering the amount of HCl-extractable Fe(II) depleted in the setup with pyrite and ^{57}Fe-siderite (Table S2),

up to 0.2 mM of sulfate deriving from oxidation of structural sulfur (S_2^{2-}) could be produced by Fe^{3+} driven oxidation of pyrite.

$$FeS_2 + 14Fe^{3+} + 8H_2O \rightarrow Fe^{2+} + 2SO_4^{2-} + 16H^+ \qquad (3)$$

Considering this value (0.2 mM) in addition to the theoretical concentration of sulfate which could be formed as a consequence of S^0 oxidation (0.54 mM, see above), the theoretically expected value (ca. 0.74 mM sulfate coming from oxidation of S^0 and S_2^{2-} by Fe^{3+}) is higher than the range of the measured values of total sulfate (0.60±0.10 and 0.61±0.10 for setups with pyrite and ^{57}Fe-siderite or ^{NA}Fe-siderite, respectively; Fig. 3H). These results, together with the model output, suggest that direct biotic oxidation of pyrite took place.

References

(1) Peiffer, S.; Stubert, I. The Oxidation of Pyrite at PH 7 in the Presence of Reducing and Nonreducing Fe(III)-Chelators. *Geochim. Cosmochim. Acta* **1999**, *63* (19–20), 3171–3182. https://doi.org/10.1016/S0016-7037(99)00224-0.

(2) Berner, R. A. Sedimentary Pyrite Formation. *American Journal of Science*. American Journal of Science 1970, pp 1–23. https://doi.org/10.2475/ajs.268.1.1.

(3) Yan, R.; Kappler, A.; Muehe, E. M.; Knorr, K. Effect of Reduced Sulfur Species on Chemolithoautotrophic Pyrite Oxidation with Nitrate. *Geomicrobiol. J.* **2018**, *36* (1), 19–29.

(4) Stookey, L. L. Ferrozine-A New Spectrophotometric Reagent for Iron. *Anal. Chem.* **1970**, *42* (7), 779–781. https://doi.org/10.1021/ac60289a016.

(5) Evans, B. J.; Johnson, R. G.; Senftle, F. E.; Cecil, C. B.; Dulong, F. The 57Fe Mössbauer Parameters of Pyrite and Marcasite with Different Provenances. *Geochim. Cosmochim. Acta* **1982**, *46* (5), 761–775. https://doi.org/10.1016/0016-7037(82)90028-X.

(6) Bai, Y.; Mellage, A.; Cirpka, O. A.; Sun, T.; Angenent, L. T.; Haderlein, S. B.; Kappler, A. AQDS and Redox-Active NOM Enables Microbial Fe(III)-Mineral Reduction at Cm-Scales. *Environ. Sci. Technol.* **2020**, *54* (7), 4131–4139. https://doi.org/10.1021/acs.est.9b07134.

(7) Coleman, T. F.; Li, Y. An Interior Trust Region Approach for Nonlinear Minimization Subject to Bounds. *SIAM J. Optim.* **1996**, *6* (2), 418–445. https://doi.org/10.1137/0806023.

(8) Ehrenreich, A.; Widdel, F. Anaerobic Oxidation of Ferrous Iron by Purple Bacteria, a New Type of Phototrophic Metabolism. *Appl. Environ. Microbiol.* **1994**, *60* (12), 4517–4526. https://doi.org/10.1128/aem.60.12.4517-4526.1994.